Negative Friction Coefficients in Superlubric Graphite–Hexagonal Boron Nitride Heterojunctions

Davide Mandelli, Wengen Ouyang, Oded Hod,* and Michael Urbakh
Department of Physical Chemistry, School of Chemistry, The Raymond and Beverly Sackler Faculty of Exact Sciences and The Sackler Center for Computational Molecular and Materials Science, Tel Aviv University, Tel Aviv 6997801, Israel

(Received 12 September 2018; revised manuscript received 3 December 2018; published 21 February 2019)

Negative friction coefficients, where friction is reduced upon increasing normal load, are predicted for superlubric graphite–hexagonal boron nitride heterojunctions. The origin of this counterintuitive behavior lies in the load-induced suppression of the moiré superstructure out-of-plane distortions leading to a less dissipative interfacial dynamics. Thermally induced enhancement of the out-of-plane fluctuations leads to an unusual increase of friction with temperature. The highlighted frictional mechanism is of a general nature and is expected to appear in many layered material heterojunctions.

DOI: 10.1103/PhysRevLett.122.076102

Energy dissipation, wear, and the ensuing failure of moving components are problems encountered in many human activities. Reducing friction is of particular importance in microscopic and nanoscopic mechanical devices [1], where the damaging consequences of local heating are amplified by the large surface-to-volume ratio. Standard lubrication schemes may fail in these extremely confined conditions, which calls for novel alternative solutions [2], such as dry solid coatings. In this approach, frictional forces are reduced thanks to the effective cancellation of lateral interactions occurring between incommensurate rigid crystalline surfaces. This phenomenon, often termed structural superlubricity, was first proposed theoretically a few decades ago [3] as a way to achieve extremely low friction coefficients [4–7]. Despite the fact that structural superlubricity has been observed in different material contacts [8–12], its implementation in practical solid-solid lubrication schemes remains a challenging task. Nevertheless, recent breakthrough demonstrations [13–17], based on van der Waals heterojunctions, suggest that this goal may be within our reach.

Among the family of layered compounds, junctions formed between graphite and hexagonal boron nitride (*h*-BN) have been predicted as promising candidates to achieve robust superlubricity [18,19]. This was recently verified experimentally for micron-sized monocrystalline interfaces [16], where superlubricity was found to persist even under ambient conditions and over a broad range of sliding velocities. However, due to experimental restrictions, measurements were performed only at relatively small applied normal pressures of $\lesssim$10 MPa.

In this Letter, we use molecular dynamics simulations to investigate the frictional response of extended graphite–*h*-BN contacts under uniform normal loads up to ~10 GPa. Using state-of-the-art interlayer force fields we show that superlubricity persists across the entire range of normal loads investigated. Surprisingly, we find that kinetic friction displays a nonmonotonic behavior with external load, where an initial regime of friction reduction (by up to ~30% relative to the zero-load value) is followed by friction increase for higher normal loads. These negative friction coefficients (NFCs) originate from the load-induced suppression of energy dissipation via out-of-plane atomic motion. This behavior is expected to appear in many heterogeneous two-dimensional material interfaces that possess a corrugated moiré superstructure and exhibit superlubric motion.

Our main goal is to investigate the frictional response of layered graphene–*h*-BN heterojunctions over a broad range of normal loads and identify conditions where NFCs can be obtained. To this end, we consider the model system presented in Fig. 1(a). Here, a laterally periodic graphene monolayer is aligned over a substrate made of four *h*-BN layers, with parallel crystalline axes. The carbon-carbon and boron-nitrogen intralayer interactions are modeled via the REBO [20,21] and the Tersoff [22] potentials, respectively. The interlayer interactions are described via the graphene–*h*-BN interlayer potential [23,24]. This model describes well the frictional behavior of realistic three-dimensional graphite–*h*-BN contacts [16]. Because of the inherent 1.8% lattice constant mismatch between graphene and *h*-BN, a moiré superstructure of period $\lambda_m \approx 14$ nm appears in the fully relaxed interface. In agreement with experiments [25], we observe a periodic sequence of extended domains, where graphene remains flat and stretches to reach local lattice commensurability with the underlying substrate, separated by narrow domain walls, where in-plane compressive strain is accumulated [see Fig. 1(b)]. The latter is partially relieved via the formation of elevated ridges [see Fig. 1(c)] that minimize the total energy by converting energetically costly in-plane compressions into cheaper local out-of-plane distortions

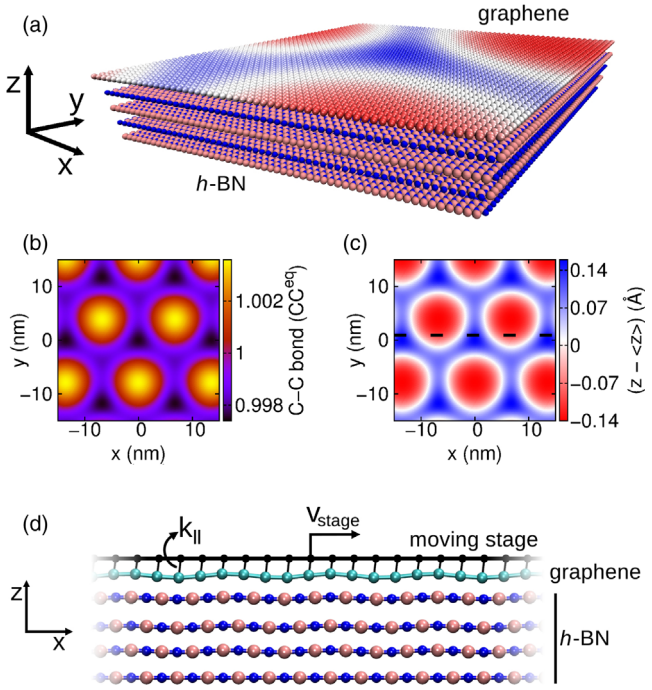

FIG. 1. (a) The model heterojunction: a graphene monolayer aligned over a four-layer thick h-BN substrate with rigid bottom layer. Carbon atoms are colored according to their vertical position with respect to the average basal plane of the graphene layer, where blue and red correspond to the maximum and minimum values attained, respectively. The scale bar is the same as in panel c. (b) Colored map of the average carbon-carbon distance (in units of the equilibrium bond-length) after relaxation of the graphene layer over h-BN at zero normal load. (c) The corresponding colored map of the out-of-plane distortions of graphene. (d) Schematics of the simulations setup: the graphene layer is attached to a rigid stage moving at fixed velocity of v_{stage} along the x direction. Driving forces are exerted via identical springs of elastic constant $k_{\parallel}$ acting only parallel to the substrate. No forces are exerted by the springs in the normal direction. The perpendicular position of the stage is shifted vertically for clarity of the presentation. Carbon, boron, and nitrogen atoms are represented by cyan, pink, and blue spheres, respectively.

(see Sec. 1 of the Supplemental Material [26] for details). This structure may present friction coefficients well within the superlubric regime [15,16,18] due to the solitonlike motion [31] of the elevated moiré ridges [19].

To model the effects of external load on friction, we perform fully atomistic dynamic simulations, where the graphene layer is attached to a stage moving at constant velocity [see Fig. 1(d)], mimicking recent sliding friction experiments of microscale graphite–h-BN contacts [16]. The stage is modeled as a rigid flat duplicate of the graphene slider and the normal load is simulated by applying a uniform force to all slider atoms, vertical to the graphene basal plane and pressing towards the h-BN substrate. In realistic scenarios this can be achieved by a sufficiently thick slider, which helps spreading the load evenly across the interface [16]. The equations of motion for the carbon atoms are given by

$$m_C\ddot{\boldsymbol{r}}_i = -\boldsymbol{\nabla}_{\boldsymbol{r}_i}(V_{\mathrm{inter}} + V_{\mathrm{intra}}) + k_{\parallel}(\boldsymbol{r}_{\parallel,i}^{\mathrm{stage}} - \boldsymbol{r}_{\parallel,i}) - F_{\mathrm{N}}\hat{z} - m_{\mathrm{C}}\sum_{\alpha=x,y,z}\eta_\alpha v_{\alpha,i}\hat{\boldsymbol{\alpha}}, \quad (1)$$

where the first two terms on the right-hand-side are the forces due to the inter- and intralayer interactions, the third term is the lateral elastic driving force due to the moving stage, the fourth term is the applied normal load, and the last term is a viscous force that accounts for energy dissipation, needed to reach steady state [32]. Similar equations are solved for the motion of the boron and nitrogen atoms within the mobile h-BN substrate layers, with the absence of the driving term and the normal load. All atoms are free to move in any direction, apart from those of the bottommost h-BN layer, which are held fixed at their equilibrium positions, and those of the moving stage that are rigidly shifted in the x direction at a constant velocity. The anisotropic nature of the system is expected to affect the rate of kinetic energy dissipation in different directions. Previous studies predicted that the vertical damping coefficient can be much larger than the lateral ones [33,34]; hence we fixed $\eta_x = \eta_y = 0.1$ and $\eta_z = 4.5\ \mathrm{ps}^{-1}$. These parameters, which fall within the typical range used in molecular dynamics simulations of nanoscale friction [32], provide good agreement with experimental data on the anisotropy of superlubric graphite–h-BN heterojunctions [16] and are close to theoretical estimations for atomic adsorbates [35]. The kinetic frictional stress σ_k is evaluated as the time average of the total shear force acting on the moving stage in the sliding direction, normalized to contact area A,

$$\sigma_k = \frac{\langle\sum_{i=1}^{N_{\mathrm{C}}} k_{\parallel}(x_i^{\mathrm{stage}} - x_i)\rangle}{A}. \quad (2)$$

Here, N_{C} is the number of slider carbon atoms, x_i and x_i^{stage} are the positions of the ith carbon atom and of its counterpart in the moving stage, respectively, and $k_{\parallel} = 11\ \mathrm{meV/\AA^2}$ is the spring constant (see further simulation details in Supplemental Material [26], Secs. 2 and 3).

The main results of our study are presented in Fig. 2, showing nonmonotonic variation of the frictional stress with respect to the applied normal load at zero and room temperature, resulting in NFCs. Considering first the zero temperature results (red curve) we find that up to an external pressure of ~5 GPa the frictional stress steadily reduces by ~20% from ~2.4 down to ~1.9 MPa. Further increase of the external load results in an increase in the frictional stress up to ~2.1 MPa obtained at the highest load investigated of ~12 GPa. This latter observation is in qualitative agreement with recent experimental results

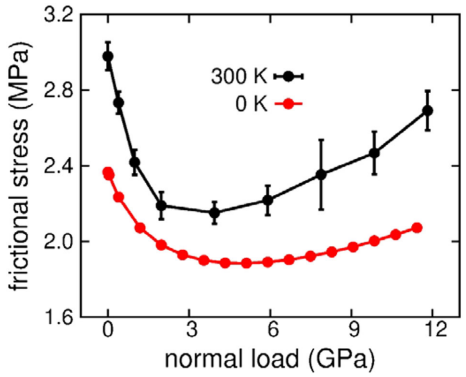

FIG. 2. Load dependence of the frictional stress obtained at zero (red) and room (black) temperature. Standard error bars are computed by block averaging.

showing linear increase of friction of graphene coated microspheres [15] or graphite flake wrapped AFM tips [17] sliding atop h-BN.

The corresponding differential friction coefficients are obtained by performing a numerical two-point derivative of the data yielding kinetic friction coefficients in the range of $-2.5\times10^{-4}<\mu_k<5\times10^{-5}$, well within the superlubric regime, defined by $\mu_k<10^{-3}$ [2]. Simulations performed at room temperature (black curves) yielded a similar frictional stress reduction of $27\pm5\%$ relative to the zero-load value (see Sec. 4 of the Supplemental Material [26] for further details). In striking difference from standard frictional scenarios, where friction reduces with increasing temperature [32], in the present case friction is found to enhance with temperature. We note that while our simulations are performed under uniform normal load, similar effects are expected to appear also for nonuniform load distributions as long as the local load does not exceed the turnover value, above which kinetic friction starts to increase.

The mechanism underlying this counterintuitive behavior can be unveiled by investigating the dependence of the different energy dissipation routes on the applied normal load. Hence, we calculate the steady-state frictional power, p_{fric}, dissipated at zero temperature, from which the kinetic frictional stress can be evaluated as follows [36]:

$$\sigma_k = p_{\mathrm{fric}}/Av_{\mathrm{stage}} = (p_{\mathrm{com}} + p_{\mathrm{internal}})/Av_{\mathrm{stage}}. \quad (3)$$

Here,

$$p_{\mathrm{com}} = \sum_{i=1}^{N_{\mathrm{layers}}} M_i \sum_{\alpha=x,y,z} \eta_\alpha \langle (v^i_{\alpha,\mathrm{com}}(t))^2 \rangle \quad (4)$$

is the time-averaged power dissipated by the center-of-mass degree of freedom (d.o.f.) of each layer, where N_{layers} is the total number of layers, M_i is the total mass of the ith layer, and $v^i_{\alpha,\mathrm{com}}$ is its center-of-mass velocity along Cartesian direction $\alpha=x,y,z$. p_{internal} accounts for the power dissipated through the motion of the internal d.o.f. in the center-of-mass reference frame, and is given by

$$p_{\mathrm{internal}} = \sum_{i=1}^{N_{\mathrm{layers}}} \sum_{k=1}^{N_i} m^i_k \sum_{\alpha=x,y,z} [\eta_\alpha \langle (v^i_{\alpha,k}(t) - v^i_{\alpha,\mathrm{com}}(t))^2 \rangle], \quad (5)$$

where N_i is the number of atoms in the ith layer and m^i_k and $v^i_{\alpha,k}$ are the mass and α Cartesian velocity component of the kth atom in that layer, respectively.

Figure 3(a) reports the center-of-mass contribution to dissipation obtained at 0 K, which is dominated by its component along the sliding direction [black curve in Fig. 3(a)]. Notably, the center-of-mass dissipation shows no significant load dependence suggesting that the origin of the NFCs reported above lies within the dynamics of the internal d.o.f. of the slider. To verify this, we show in Fig. 3(b) the overall contributions from the internal d.o.f. of all layers at zero temperature. We observe that this is dominated by the vertical component [red curve in Fig. 3(b)], which displays the reported nonmonotonic trend. We further note that over 90% of the energy dissipated is associated with the motion of the upper graphene layer (see Supplemental Material [26], Sec. 6). Therefore, the nonmonotonic frictional behavior stems from the effect of normal load on the out-of-plane motion of the graphene atoms.

Performing similar analysis at room temperature is more delicate, since the statistical errors in the frictional power are much larger than the overall average frictional stress. Nevertheless, the similar trends obtained for the frictional stress at zero and room temperatures (see Fig. 2) suggest that the same physical mechanism underlies the observed nonmonotonic behavior in both cases. Furthermore, the thermally induced enhancement of the out-of-plane fluctuations explains the unusual increase of friction with temperature.

The key to understand the obtained NFCs is to study the dependence of the moiré ridge structure and its solitonlike

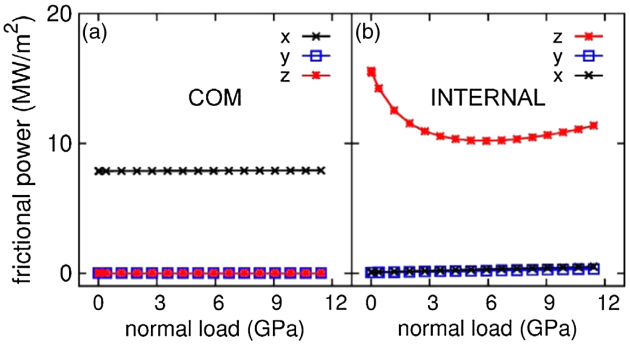

FIG. 3. Load dependence of the frictional power dissipated at zero temperature by (a) the center of mass and (b) the internal d.o.f. of all model heterojunction mobile layers.

dynamics on the applied external load [16,19]. In Fig. 4(a) we present the ridge profile as obtained at three normal load values: zero load, ∼4 GPa (where the friction stress obtains a minimum), and ∼11 GPa. The profile is taken along a scan line in the sliding direction that corresponds to the maximum peak-dip value of the vertical deformations of graphene [see dashed black line in Fig. 1(c)]. We observe a strong initial decrease of the ridge peak height accompanied by its narrowing when the load increases up to 4 GPa [see also Fig. 4(b)]. Further increasing the pressure to ∼11 GPa results in merely mild reduction of the ridge peak height with additional narrowing of its width. This behavior results from the fact that at the peak region the system is forced into an unfavorable interlayer stacking, whereas at the flat regions the layers assume nearly optimal stacking (see Supplemental Material [26], Sec. 1). Hence, the reduction of the peak height at larger external loads requires a higher energy penalty as compared to the flat regions.

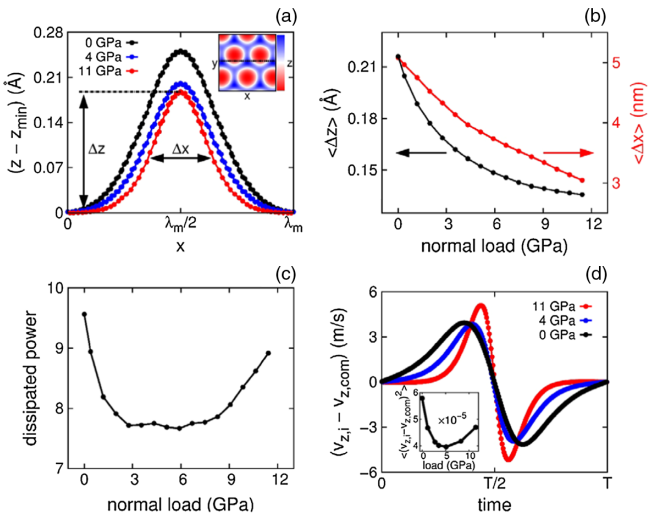

FIG. 4. Mechanism of NFCs. (a) The moiré superstructure ridge cross section at an applied pressure of 0 (black), 4 (blue), and 11 (red) GPa. The scan line (see inset) corresponds to the maximum peak-dip value of the vertical deformations of graphene along the direction of sliding x, expressed in units of the moiré periodicity of $\lambda_m \approx 14$ nm. The definitions of the maximum height Δz and the full-width-at-half-maximum Δx are marked by the double-headed arrows. (b) Load dependence of the characteristic peak-dip value Δz (black) and full-width-at-half-maximum Δx (red) of the moiré ridge. (c) Load dependence of the normalized power dissipated via vertical motion obtained from the simplistic model (see Supplemental Material [26], Sec. 7 for further details). (d) Vertical velocity of the carbon atom, which displays the largest velocity fluctuations during sliding under applied normal pressures of 0 (black), 4 (blue), and 11 (red) GPa, measured within the slider's center-of-mass reference frame. Time is expressed in units of the period of the trajectory at steady state $T = a_{h-\mathrm{BN}}/v_{\mathrm{stage}} \approx 25$ ps. Inset: Load dependence of the time-averaged value of $\langle (v_{z,i} - v_{z,\mathrm{com}})^2 \rangle$, proportional to the energy dissipation, where $v_{z,i}$ is the given atom vertical velocity.

To evaluate the effect of slider thickness, we have performed geometry optimizations of a stack of six graphene layers atop six h-BN layers under external load and found a similar load-dependence of the moiré vertical distortions (see Supplemental Material [26], Sec. 5), thus indicating the validity of the graphene monolayer model adopted herein. Furthermore, we expect that relaxing the periodic boundary conditions, valid for large-scale monocrystalline interfaces [16], will allow for more pronounced load induced flattening of the moiré ridges resulting in larger absolute NFCs.

These findings can now be used to construct a simplistic model, based on geometric arguments, that captures all physical characteristics required to reproduce the NFCs phenomenon. We recall that the frictional response is dominated by energy dissipation due to the out-of-plane motion of the graphene layer. The corresponding vertical velocity of the carbon atoms due to the ridge solitonlike motion can be estimated as $v_z^{\max} \approx \Delta z/\Delta t$, where Δz is the moiré ridge height and Δt is the typical passage time of the domain wall during sliding. The latter can be estimated as $\Delta t \approx \Delta x/2v_m$, where $\Delta x/2$ and v_m are half of the ridge width at half height and the sliding velocity of the moiré pattern, respectively. To evaluate v_m, we note that if the graphene layer is displaced by one substrate lattice spacing, $a_{h-\mathrm{BN}}$, the final configuration is undistinguishable from the initial one; hence, the moiré ridge must have moved by λ_m. Therefore, the superstructure propagation velocity is given by $v_m \approx (\lambda_m/a_{h-\mathrm{BN}})v_{x,\mathrm{com}} \approx 50 v_{x,\mathrm{com}}$, where $v_{x,\mathrm{com}}$ is the velocity of the center of mass of the graphene layer in the sliding direction. Finally, the dissipated power in Eq. (5) can be estimated as $m_C\eta_z(v_z^{\max})^2 = 4m_C(\lambda_m v_{x,\mathrm{com}}/a_{h-\mathrm{BN}})^2\eta_z(\Delta z/\Delta x)^2$. Figure 4(c) presents the load dependence of this expression using the height and width variations appearing in Fig. 4(b). To obtain a dimensionless parameter, we normalize the results by the characteristic power dissipated via the translational d.o.f. in the sliding direction $m_C\eta_x v_{\mathrm{stage}}^2$. Clearly, the simplistic model reproduces well the nonmonotonic load dependence of the friction force leading to the NFCs, including an overall 20% frictional reduction between 0 and ∼5 GPa. We note that in the range of high normal loads (above the turnover point) the simplistic model exhibits somewhat larger frictional increase than the direct atomistic simulations. This can be attributed to the fact that the variations of the characteristic ridge height become smaller for increasing normal load, thus affecting the accuracy of the model.

The qualitative explanation given by this model regarding the pressure dependence of the vertical carbon atoms' velocity is further supported by our simulations. Figure 4(d) shows a typical vertical velocity temporal profile of a carbon atom within the graphene layer. The

average magnitude of the vertical velocity first reduces with the increase of pressure from 0 to 4 GPa. However, further increase of the external pressure to 11 GPa results in sharpening of the ridge regions, as explained above, yielding increasing vertical velocities. The corresponding time average of the square vertical velocity $\langle (v_{z,i} - v_{z,\mathrm{com}})^2 \rangle$, which provides a measure of the energy dissipated via out-of-plane atomic motion, correlates well [see inset in Fig. 4(d)] with the nonmonotonic behavior of the friction force presented above.

Therefore, we now have a simple and clear understanding of the physical mechanism underlying the NFCs predicted to appear in extended monocrystalline graphite–*h*-BN heterojunctions. Out-of-plane atomic motion plays a key role in this effect. Specifically, the competition between height reduction and narrowing of the moiré superstructure ridges under external pressure leads to an initial reduction of the magnitude of the slider atoms' vertical velocities followed by their subsequent increase. This leads to a nonmonotonic load dependence of the interfacial frictional dissipation and its unusual temperature dependence. Notably, recent theoretical predictions and experimental observations reported NFCs for atomic force microscopy tips sliding atop graphitic surfaces [37–40]. However, the origin of NFCs in these studies was identified as partial delamination of the substrate under tip retraction [37] or the reduction of surface puckering with increasing load in suspended systems [38–40]. Furthermore, a recent computational study predicted NFCs in homogeneous monocrystalline MoS_2 contacts due to flattening of the sliding potential energy surface under extremely high loads [41]. The unique mechanism that we predict herein is of general nature, emerges at moderate external loads, and should apply to many other layered material heterojunctions when placed in an aligned configuration. With this respect, increasing the interfacial misfit angle results in rapid reduction of the amplitude of the out-of-plane corrugation; hence, the predicted NFCs effect is expected to become less pronounced.

We can therefore conclude that in order to achieve NFCs within the suggested mechanism the interface should (i) be *superlubric* to avoid center-of-mass stick-slip motion, (ii) be *anisotropic* with high intralayer stiffness and low bending rigidity to allow for the formation of a corrugated superstructure (see, e.g., MoS_2/WSe_2 interfaces, for which large out-of-plane distortions of up to $\Delta z \approx 1$ Å have been predicted [42,43]), (iii) be held at an aligned configuration to achieve large-scale corrugated moiré superstructure, and (iv) exhibit *solitonlike* superstructure motion under shear stress. With this respect it is interesting to note that a moiré pattern characterized by vertical distortions of the order of $\Delta z \approx 0.1$ Å is expected to appear for small misalignment angles also in homogeneous graphitic contacts [44,45], suggesting that NFCs may be observed in twisted bilayer graphene, as well.

D. M. acknowledges support from the Sackler Center for Computational Molecular and Materials Science at Tel Aviv University, and from Tel Aviv University Center for Nanoscience and Nanotechnology. W. O. acknowledges the financial support of the Fellowship Program for Outstanding Post-Doctoral Researchers from China and India provided by the Israel Council for Higher Education's Planning and Budgeting Committee. M. U. acknowledges the financial support of the Israel Science Foundation, Grant No. 1141/18, and of the Deutsche Forschungsgemeinschaft (DFG), Grant No. BA 1008/21-1. O. H. is grateful for the generous financial support of the Israel Science Foundation under Grant No. 1586/17 and the Naomi Foundation for generous financial support via the Kadar Award. This work is supported in part by COST Action MP1303.

*odedhod@tauex.tau.ac.il

[1] J. A. Williams and H. Le, J. Phys. D **39**, R201 (2006).
[2] A. Erdemir and J.-M. Martin, *Superlubricity* (Elsevier, New York, 2007).
[3] K. Shinjo and M. Hirano, Surf. Sci. **283**, 473 (1993).
[4] O. Hod, E. Meyer, Q. Zheng, and M. Urbakh, Nature (London) **563**, 485 (2018).
[5] J. M. Martin and A. Erdemir, Phys. Today **71**, No. 4, 40 (2018).
[6] D. Berman, A. Erdemir, and A. V. Sumant, ACS Nano **12**, 2122 (2018).
[7] M. Z. Baykara, M. R. Vazirisereshk, and A. Martini, Appl. Phys. Rev. **5**, 041102 (2018).
[8] J. M. Martin, C. Donnet, T. Le Mogne, and T. Epicier, Phys. Rev. B **48**, 10583 (1993).
[9] M. Hirano, K. Shinjo, R. Kaneko, and Y. Murata, Phys. Rev. Lett. **78**, 1448 (1997).
[10] M. Dienwiebel, G. S. Verhoeven, N. Pradeep, J. W. M. Frenken, J. A. Heimberg, and H. W. Zandbergen, Phys. Rev. Lett. **92**, 126101 (2004).
[11] Z. Liu, J. Yang, F. Grey, J. Z. Liu, Y. Liu, Y. Wang, Y. Yang, Y. Cheng, and Q. Zheng, Phys. Rev. Lett. **108**, 205503 (2012).
[12] J. Yang, Z. Liu, F. Grey, Z. Xu, X. Li, Y. Liu, M. Urbakh, Y. Cheng, and Q. Zheng, Phys. Rev. Lett. **110**, 255504 (2013).
[13] E. Koren, C. Rawlings, A. W. Knoll, and U. Duerig, Science **348**, 679 (2015).
[14] D. Berman, S. A. Deshmukh, S. K. R. S. Sankaranarayanan, A. Erdemir, and A. V. Sumant, Science **348**, 1118 (2015).
[15] S.-W. Liu, H.-P. Wang, Q. Xu, T.-B. Ma, G. Yu, C. Zhang, D. Geng, Z. Yu, S. Zhang, W. Wang, Y.-Z. Hu, H. Wang, and J. Luo, Nat. Commun. **8**, 14029 (2017).
[16] Y. Song, D. Mandelli, O. Hod, M. Urbakh, M. Ma, and Q. Zheng, Nat. Mater. **17**, 894 (2018).
[17] Y. Liu, A. Song, Z. Xu, R. Zong, J. Zhang, W. Yang, R. Wang, Y. Hu, J. Luo, and T. Ma, ACS Nano **12**, 7638 (2018).
[18] I. Leven, D. Krepel, O. Shemesh, and O. Hod, J. Phys. Chem. Lett. **4**, 115 (2013).

[19] D. Mandelli, I. Leven, O. Hod, and M. Urbakh, Sci. Rep. **7**, 10851 (2017).
[20] S. J. Stuart, A. B. Tutein, and J. A. Harrison, J. Chem. Phys. **112**, 6472 (2000).
[21] D. W. Brenner, O. A. Shenderova, J. A. Harrison, S. J. Stuart, B. Ni, and S. B. Sinnott, J. Phys. Condens. Matter **14**, 783 (2002).
[22] C. Sevik, A. Kinaci, J. B. Haskins, and T. Çağın, Phys. Rev. B **84**, 085409 (2011).
[23] I. Leven, T. Maaravi, I. Azuri, L. Kronik, and O. Hod, J. Chem. Theory Comput. **12**, 2896 (2016).
[24] T. Maaravi, I. Leven, I. Azuri, L. Kronik, and O. Hod, J. Phys. Chem. C **121**, 22826 (2017).
[25] C. R. Woods *et al.*, Nat. Phys. **10**, 451 (2014).
[26] See Supplemental Material at http://link.aps.org/supplemental/10.1103/PhysRevLett.122.076102 for detailed methods and supplementary results and discussions, which includes Refs. [27–30].
[27] I. Leven, R. Guerra, A. Vanossi, E. Tosatti, and O. Hod, Nat. Nanotechnol. **11**, 1082 (2016).
[28] A. N. Kolmogorov and V. H. Crespi, Phys. Rev. B **71**, 235415 (2005).
[29] E. Bitzek, P. Koskinen, F. Gähler, M. Moseler, and P. Gumbsch, Phys. Rev. Lett. **97**, 170201 (2006).
[30] W. Ouyang, D. Mandelli, M. Urbakh, and O. Hod, Nano Lett. **18**, 6009 (2018).
[31] A. Vanossi, N. Manini, and E. Tosatti, Proc. Natl. Acad. Sci. U.S.A. **109**, 16429 (2012).
[32] A. Vanossi, N. Manini, M. Urbakh, S. Zapperi, and E. Tosatti, Rev. Mod. Phys. **85**, 529 (2013).
[33] B. N. J. Persson and R. Ryberg, Phys. Rev. B **32**, 3586 (1985).
[34] B. N. J. Persson, E. Tosatti, D. Fuhrmann, G. Witte, and C. Wöll, Phys. Rev. B **59**, 11777 (1999).
[35] B. N. J. Persson, *Sliding Friction* (Springer, Berlin, Heidelberg, 1998).
[36] M. Weiss and F.-J. Elmer, Z. Phys. B **104**, 55 (1997).
[37] Z. Deng, A. Smolyanitsky, Q. Li, X.-Q. Feng, and R. J. Cannara, Nat. Mater. **11**, 1032 (2012).
[38] Z. Deng, N. N. Klimov, S. D. Solares, T. Li, H. Xu, and R. J. Cannara, Langmuir **29**, 235 (2013).
[39] A. Smolyanitsky and J. P. Killgore, Phys. Rev. B **86**, 125432 (2012).
[40] Z. Ye and A. Martini, Langmuir **30**, 14707 (2014).
[41] J. Sun, Y. Zhang, Z. Lu, Q. Li, Q. Xue, S. Du, J. Pu, and L. Wang, J. Phys. Chem. Lett. **9**, 2554 (2018).
[42] C. Zhang, C.-P. Chuu, X. Ren, M.-Y. Li, L.-J. Li, C. Jin, M.-Y. Chou, and C.-K. Shih, Sci. Adv. **3**, e1601459 (2017).
[43] H. Yu, G.-B. Liu, J. Tang, X. Xu, and W. Yao, Sci. Adv. **3**, e1701696 (2017).
[44] M. M. van Wijk, A. Schuring, M. I. Katsnelson, and A. Fasolino, 2D Mater. **2**, 034010 (2015).
[45] G. Li, A. Luican, J. M. B. Lopes dos Santos, A. H. Castro Neto, A. Reina, J. Kong, and E. Y. Andrei, Nat. Phys. **6**, 109 (2010).